

# Templated-Construction of Hollow MoS<sub>2</sub> Architectures with Improved Photoresponses

Chao Gao, Yingdong Han, Kun Zhang, Tian Wei, Zhang Jiang, Yang Wei, Lisha Yin, Fabio Piccinelli, Cheng Yao, Xiaoji Xie,\* Marco Bettinelli, and Ling Huang\*

Despite the outstanding optoelectronic properties of MoS<sub>2</sub> and its analogues, synthesis of such materials with desired features including fewer layers, arbitrary hollow structures, and particularly specifically customized morphologies, via inorganic reactions has always been challenging. Herein, using pre-designed lanthanide-doped upconversion luminescent materials (e.g., NaYF<sub>4</sub>:Ln) as templates, arbitrary MoS<sub>2</sub> hollow structures with precisely defined morphologies, widely variable dimensions, and very small shell thickness ( $\approx 2.5$  nm) are readily constructed. Most importantly, integration of the near-infrared-responsive template significantly improves the photoresponse of up to 600 fold in device made of NaYF<sub>4</sub>:Yb/Er@MoS<sub>2</sub> compared with that of MoS<sub>2</sub> nanosheets under 980 nm laser illumination. Multichannel optoelectronic device is further fabricated by simply changing luminescent ions in the template, e.g., NaYF<sub>4</sub>:Er@MoS<sub>2</sub>, operating at 1532 nm light excitation with a 276-fold photoresponse enhancement. The simple chemistry, easy operation, high reliability, variable morphologies, and wide universality represent the most important advantages of this novel strategy that has not been accessed before.

potentials in many applications including host materials for energy storage in metal ion batteries and super capacitors, catalysts for hydrogen evolution reactions, as well as devices for gas sensors, flash memories, and photodetectors.<sup>[1–10]</sup>


In virtue of its sandwich-like structure coupled by van der Waals forces and the in-plan S–Mo–S covalent bonding, numerous efforts have been invested aiming to exfoliate bulk MoS<sub>2</sub> into single or few-layered sheets to satisfy different requirements.<sup>[11,12]</sup> However, one of the serious challenges is that the exfoliated nanosheets are prone to reaggregate or restack when extracted from solution, causing even massier piling, such as twisted, folded, or broken pieces and resulting in significantly deteriorated performance.<sup>[13–15]</sup> Thus, MoS<sub>2</sub> architectures with large surface area, particularly those hollow structures with precisely designable and retainable configurations are highly demanded.<sup>[16–18]</sup> For example,

As a shining star among two-dimensional transition metal dichalcogenides (TMDs), MoS<sub>2</sub> and its composites have aroused impressive research enthusiasms due to their outstanding physical and chemical properties, such as large surface area, excellent electric conductivity, adjustable band gap, and tailorable density of active sites. Such superior features have imparted them great

Li et al. synthesized  $\approx 100$  nm thick hollow microcube framework of MoS<sub>2</sub> with high specific capacity and large electrolyte/electrode contact for sodium storage.<sup>[16]</sup> Zhuo et al. constructed hierarchical MoS<sub>2</sub> nanotubes with a layer thickness of  $\approx 50$  nm through anion exchange and improved photocurrent was obtained;<sup>[17]</sup> Yu et al. fabricated cubic hollow MoS<sub>2</sub> structures with a thickness

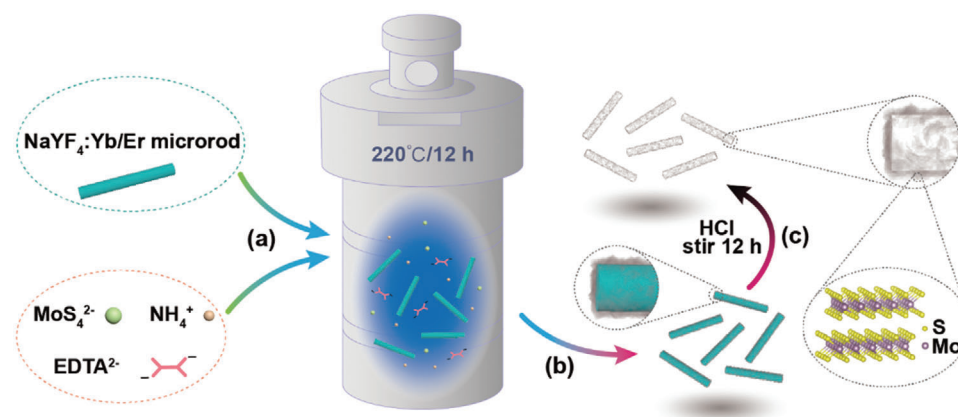
Dr. C. Gao, Dr. K. Zhang, T. Wei, Z. Jiang, Y. Wei, Dr. L. Yin, Prof. X. Xie, Prof. L. Huang  
Institute of Advanced Materials (IAM)  
Jiangsu National Synergetic Innovation Center for Advanced Materials (SICAM)  
Nanjing Tech University  
30 South Puzhu Road, Nanjing 211816, China  
E-mail: iamxjie@njtech.edu.cn; iamlhuan@njtech.edu.cn

Dr. C. Gao  
School of Inspection and Testing Certification  
Changzhou Vocational Institute of Engineering  
Changzhou 213164, China  
Dr. Y. Han  
School of Precision Instruments and Optoelectronics Engineering  
Tianjin University  
Tianjin 300072, China  
Prof. F. Piccinelli, Prof. M. Bettinelli  
Luminescent Materials Laboratory  
Department of Biotechnology  
University of Verona  
Verona 37134, Italy  
Prof. C. Yao  
School of Chemistry and Molecular Engineering  
Nanjing Tech University  
30 South Puzhu Road Nanjing 211816, China

 The ORCID identification number(s) for the author(s) of this article can be found under <https://doi.org/10.1002/adv.202002444>

© 2020 The Authors. Published by Wiley-VCH GmbH. This is an open access article under the terms of the Creative Commons Attribution License, which permits use, distribution and reproduction in any medium, provided the original work is properly cited.

DOI: 10.1002/adv.202002444



**Scheme 1.** Schematic illustration of the synthetic procedures of hollow MoS<sub>2</sub> architectures. a) Preparation of reacting ingredients inside an autoclave, b) synthesized composites, and c) microtubes obtained after removal of template.

of  $\approx 20$  nm, aiming at maximizing the exposed edge sites to promote its catalytic activity.<sup>[18]</sup> Nonetheless, those architectures are still tens or hundreds of times thicker than the value (6.5 Å) characteristic of a single layer MoS<sub>2</sub>,<sup>[8]</sup> and there remains a large room for further improving the ratio of exposed surface area to the mass of MoS<sub>2</sub>. Thus, hollow structures with even thinner shells possessing large surface-to-volume ratio, high percentage of exposed atoms, customizable morphologies, and thus better performance in electrochemical catalysis and enhanced sensitivities in optoelectronic devices are highly desired.

Meanwhile, although lanthanide-doped upconversion luminescent materials have been thoroughly studied for their unique optical response under near-infrared (NIR) illumination,<sup>[19–22]</sup> the simple inorganic chemistry of lanthanide fluorides for being used as template for MoS<sub>2</sub> hollow structure synthesis remains untouched. Specifically, templates with widely designable morphologies and dimensions can be easily synthesized, and they can also be neatly removed by just soaking in acidic solution.<sup>[23]</sup> Thus, a series of arbitrary MoS<sub>2</sub> hollow structures with shells as thin as  $\approx 2.5$  nm and dimensions ranging from as small as 35 nm to as large as several micrometers, can all be reliably constructed. More intriguingly, upconversion luminescence (UCL) at the wavelength of 540 and 654 nm generated by doped Yb<sup>3+</sup>/Er<sup>3+</sup> in the template under NIR light excitation (980 nm), falls completely within the absorption range of MoS<sub>2</sub> (350–950 nm), which facilitates efficient resonance energy transfer (ET) and significantly improves optoelectronic responses. Following the same design principle, it has also been possible to fabricate photodetectors working at other wavelength (1532 nm) by simply changing the luminescent ions of the template, demonstrating great potential for interdisciplinary applications.

As illustrated in **Scheme 1**, using the most thoroughly studied NaYF<sub>4</sub>:Yb/Er (18/2 mol%) as a representative template, composites of NaYF<sub>4</sub>:Yb/Er@MoS<sub>2</sub> possessing expected morphologies and dimensions are routinely obtained by mixing the presynthesized template with precursors for MoS<sub>2</sub> thin layer growth, and then submitting the resulting solution to a hydrothermal reaction. Corresponding hollow structures are left after removal of NaYF<sub>4</sub>:Yb/Er template via a facile washing of the composite using diluted aqueous solution of HCl.

**Figure 1a** shows transmission electron microscopy (TEM) image of the as-synthesized MoS<sub>2</sub> nanosheets with typical interlayer distance of 0.658 nm. The scanning electron microscopy (SEM) image in **Figure 1b** indicates high uniformity of NaYF<sub>4</sub>:Yb/Er microrods used as template for hollow MoS<sub>2</sub> microtube construction. X-ray diffraction (XRD) patterns of NaYF<sub>4</sub>:Yb/Er@MoS<sub>2</sub> matches well with those of standard XRD data of each individual component (**Figure 1c**). Both the thin layers of MoS<sub>2</sub> and the encapsulated NaYF<sub>4</sub>:Yb/Er microrods are easily seen in TEM image (**Figure 1d**), and the interface is clearly discernable in the zoomed-in TEM image (**Figure 1e**). The 0.710 nm interlayer distance in high-resolution TEM (HRTEM) image (**Figure 1f**) matches with that of MoS<sub>2</sub>. This is also highly consistent with the elemental mapping results where a sharp edge between the distribution of Y, F, and S, Mo elements at one end of the microrod is manifested (**Figure 1g**; and **Figure S1**, Supporting Information). The microtubes are then obtained after removal of NaYF<sub>4</sub>:Yb/Er template and the structural details of MoS<sub>2</sub> particularly the 0.713 nm characteristic interlayer distance are shown in **Figure 1h–j**. Compared with the value of 0.658 nm in pristine MoS<sub>2</sub>, the increased interlayer distance is likely caused by the nonplanar stacking of individual MoS<sub>2</sub> layers. It is worth emphasizing that the morphology of microtubes was well retained and almost identical to that of template. We also affirmed that the hexagonal-phase structure was maintained in both MoS<sub>2</sub> microtubes and MoS<sub>2</sub> nanosheets as indicated in the XRD data (**Figure S2**, Supporting Information). It should be noted that the peak intensity attributed to the (002) lattice plane becomes weaker in MoS<sub>2</sub> microtubes than that in MoS<sub>2</sub> nanosheets. This suggests that MoS<sub>2</sub> microtubes might have fewer layers, which is also consistent with the high transparency seen in **Figure 1h**.<sup>[24,25]</sup>

The Raman spectrum of MoS<sub>2</sub> microtubes has two characteristic peaks at 380.4 and 403.9 cm<sup>-1</sup> (**Figure S3**, Supporting Information), which correlates to the in-plane (E<sub>12g</sub><sup>1</sup>) and out-of-plane vibration (A<sub>1g</sub>) mode of hexagonal MoS<sub>2</sub>, respectively. The frequency difference between the E<sub>12g</sub><sup>1</sup> and A<sub>1g</sub> Raman modes is  $\approx 23.5$  cm<sup>-1</sup>, which suggests very few layers of the MoS<sub>2</sub> microtube and agrees with the TEM results.<sup>[26]</sup> We also performed energy dispersive spectroscopy (EDS) characterization of the

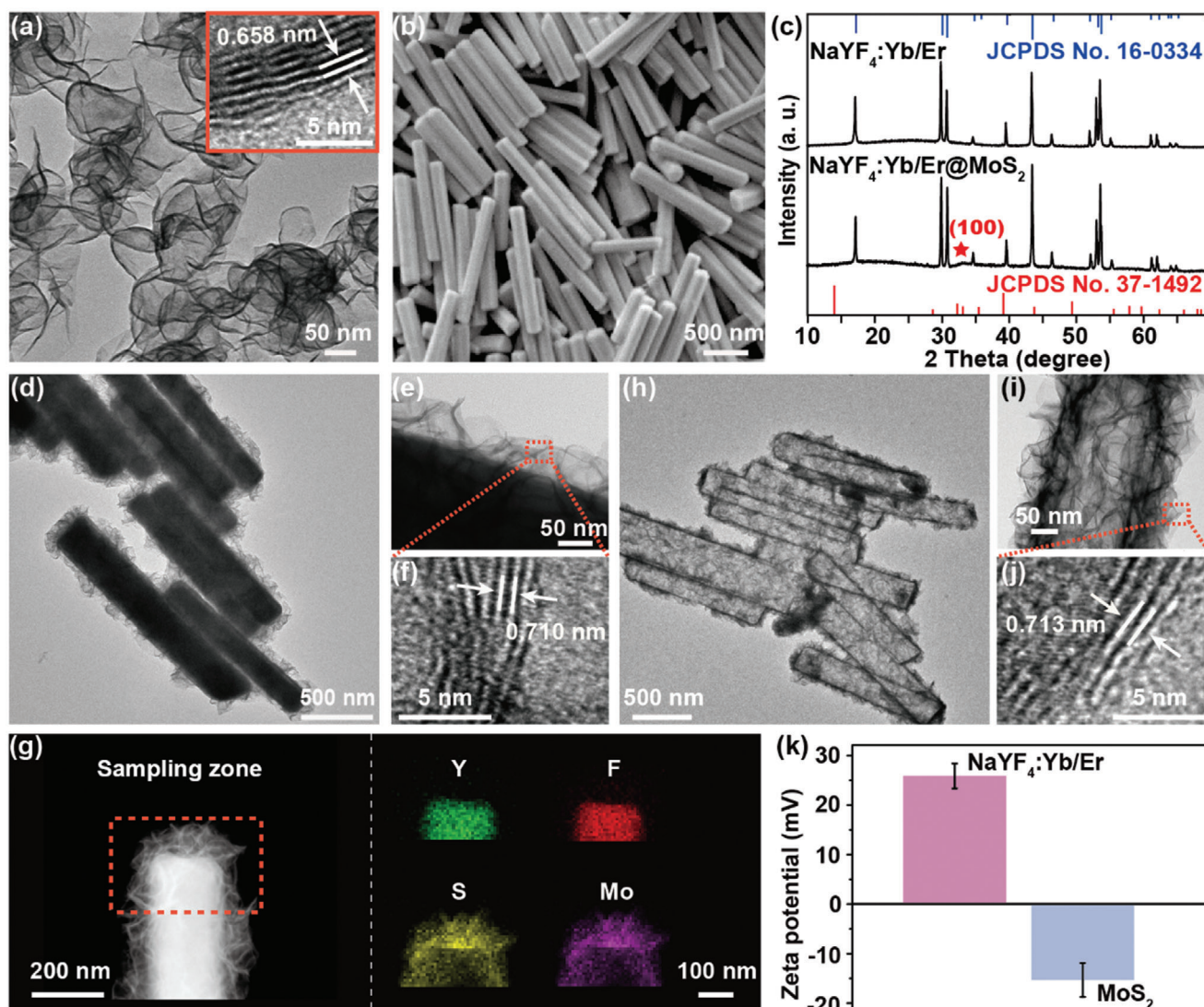


**Figure 1.** a) TEM image of as-synthesized MoS<sub>2</sub> nanosheets. b) SEM image of as-synthesized NaYF<sub>4</sub>:Yb/Er template. c) XRD patterns of NaYF<sub>4</sub>:Yb/Er@MoS<sub>2</sub> composite and NaYF<sub>4</sub>:Yb/Er microrods. The top and bottom patterns are standard XRD patterns of NaYF<sub>4</sub>:Yb/Er and MoS<sub>2</sub>, respectively. d) TEM image of NaYF<sub>4</sub>:Yb/Er@MoS<sub>2</sub> composite. e) Magnified TEM image of sample in (d). f) HRTEM image of MoS<sub>2</sub> layer in NaYF<sub>4</sub>:Yb/Er@MoS<sub>2</sub> composite shown in (e). g) Elemental mapping of the NaYF<sub>4</sub>:Yb/Er@MoS<sub>2</sub> composite showing sharp distribution of Y, F and S, Mo. h) TEM image of MoS<sub>2</sub> microtubes after removal of NaYF<sub>4</sub>:Yb/Er template. i) Magnified TEM image of sample in (h). j) HRTEM image of the edge of MoS<sub>2</sub> microtube shown in (i). k) Zeta potential profile of ligand-free NaYF<sub>4</sub>:Yb/Er microrods and as-synthesized MoS<sub>2</sub> nanosheets shown in (a).

as-synthesized hollow MoS<sub>2</sub> microtubes (Figure S4, Supporting Information), where no signals ascribable to Na<sup>+</sup>, F<sup>-</sup>, or rare earth ions (RE<sup>3+</sup>) can be detected. This indicates that the template was completely removed by soaking in aqueous HCl solution followed by a thorough wash.

Zeta potential measurement shows positive charge in NaYF<sub>4</sub>:Yb/Er template, which originates from the exposed RE<sup>3+</sup> when ligand molecules are stripped off from the microrod surface (Figure 1k).<sup>[27]</sup> The negative charge on MoS<sub>2</sub> makes it prone to combine to the surface of NaYF<sub>4</sub>:Yb/Er through electrostatic attractions, enabling natural growth of MoS<sub>2</sub> thin layers. However, since S<sup>2-</sup> is a soft base while RE<sup>3+</sup> is a hard acid according to the theory of hard and soft acids and bases formulated by Pearson,<sup>[28,29]</sup> their combination is so weak that

only small and isolated pieces of MoS<sub>2</sub> can bind randomly on NaYF<sub>4</sub>:Yb/Er surface (Figure S5, Supporting Information), resulting in poor-quality of broken MoS<sub>2</sub> hollow structures after template removal (Figure S6, Supporting Information).

To solve this problem, a surfactant molecule with stronger chelating capabilities to RE<sup>3+</sup>, i.e., a harder base, disodium salt of ethylenediamine tetraacetic acid (EDTA-2Na), was intentionally added into the reaction system. We expect that EDTA<sup>2-</sup> will bind firmly to RE<sup>3+</sup> on the template surface and meanwhile help to fix MoS<sub>2</sub> precursors (Mo<sup>6+</sup> ions) from solution and further regulate the growth of MoS<sub>2</sub> thin layers with improved quality,<sup>[30,31]</sup> when reaction conditions such as precursor concentration, reaction temperature, and growth time, are optimized. This also explains why the growth of MoS<sub>2</sub> thin layers follows so closely to

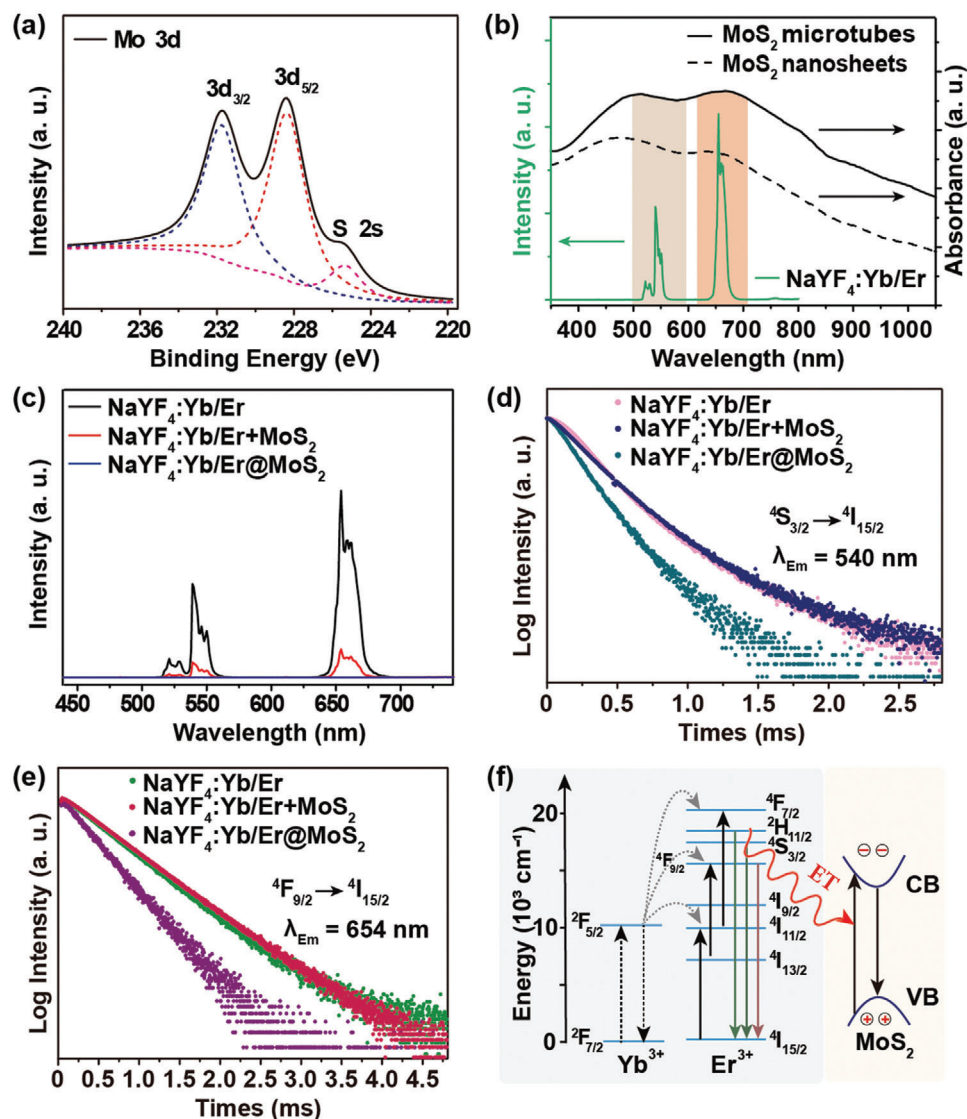


**Figure 2.** a) XPS of Mo 3d orbitals in NaYF<sub>4</sub>:Yb/Er@MoS<sub>2</sub> composite. b) UV–Vis–NIR absorption spectra of MoS<sub>2</sub> microtubes and nanosheets (right) and UCL spectrum of NaYF<sub>4</sub>:Yb/Er (left) under 980 nm laser excitation. c) UCL spectra of NaYF<sub>4</sub>:Yb/Er, NaYF<sub>4</sub>:Yb/Er+MoS<sub>2</sub>, and NaYF<sub>4</sub>:Yb/Er@MoS<sub>2</sub> composite under 980 nm laser excitation. Lifetime decay curves of NaYF<sub>4</sub>:Yb/Er, NaYF<sub>4</sub>:Yb/Er+MoS<sub>2</sub>, and NaYF<sub>4</sub>:Yb/Er@MoS<sub>2</sub> composite at emission wavelength of d) 540 and e) 654 nm. f) Proposed ET pathways from NaYF<sub>4</sub>:Yb/Er to MoS<sub>2</sub> inside the NaYF<sub>4</sub>:Yb/Er@MoS<sub>2</sub> composite.

the contour of the template (Figure 1h,i). Moreover, the very thin layer of hollow MoS<sub>2</sub> may favor higher density of active sites or electronic sensitivities than thicker analogues when used for photo- and/or electrochemical catalysis or optoelectronics.

The interactions between template and shell in NaYF<sub>4</sub>:Yb/Er@MoS<sub>2</sub> composite were further studied using X-ray photoelectron spectroscopy (XPS). The binding energies of Mo 3d<sub>3/2</sub> and Mo 3d<sub>5/2</sub> in pure MoS<sub>2</sub> nanosheets located at 232.38 and 229.18 eV shifted to 231.74 and 228.34 eV in NaYF<sub>4</sub>:Yb/Er@MoS<sub>2</sub> (Figure 2a; and Figure S7, Supporting Information), while those of S 2p<sub>1/2</sub> and S 2p<sub>3/2</sub> observed at 163.20 and 162.01 eV in pure MoS<sub>2</sub> nanosheets shifted to 162.74 and 161.54 eV (Figures S7 and S8, Supporting Information), respectively. This behavior is presumably caused by the increased electron cloud density of the outer orbitals of Mo<sup>4+</sup> and

S<sup>2-</sup> ions, which suggests the presence of a strong electrostatic interaction between MoS<sub>2</sub> and NaYF<sub>4</sub>:Yb/Er in the composite. More importantly, the respective binding energies for MoS<sub>2</sub> microtubes fell back to the values similar to those of pure MoS<sub>2</sub> nanosheets when NaYF<sub>4</sub>:Yb/Er templates were removed (Figure S7, Supporting Information), which reversely confirms the existence of electrostatic interaction.

The complete spectral overlap between the UV–Visible–NIR absorption of MoS<sub>2</sub> and the UCL emissions of NaYF<sub>4</sub>:Yb/Er under 980 nm laser excitation (Figure 2b; and Figure S9, Supporting Information) allows efficient nonradiative ET between the two components, which is reflected by the significantly decreased UCL intensity of NaYF<sub>4</sub>:Yb/Er@MoS<sub>2</sub> compared with that of pure NaYF<sub>4</sub>:Yb/Er (Figure 2c). As a control experiment, the UCL of NaYF<sub>4</sub>:Yb/Er in its physical mixture with MoS<sub>2</sub> is still

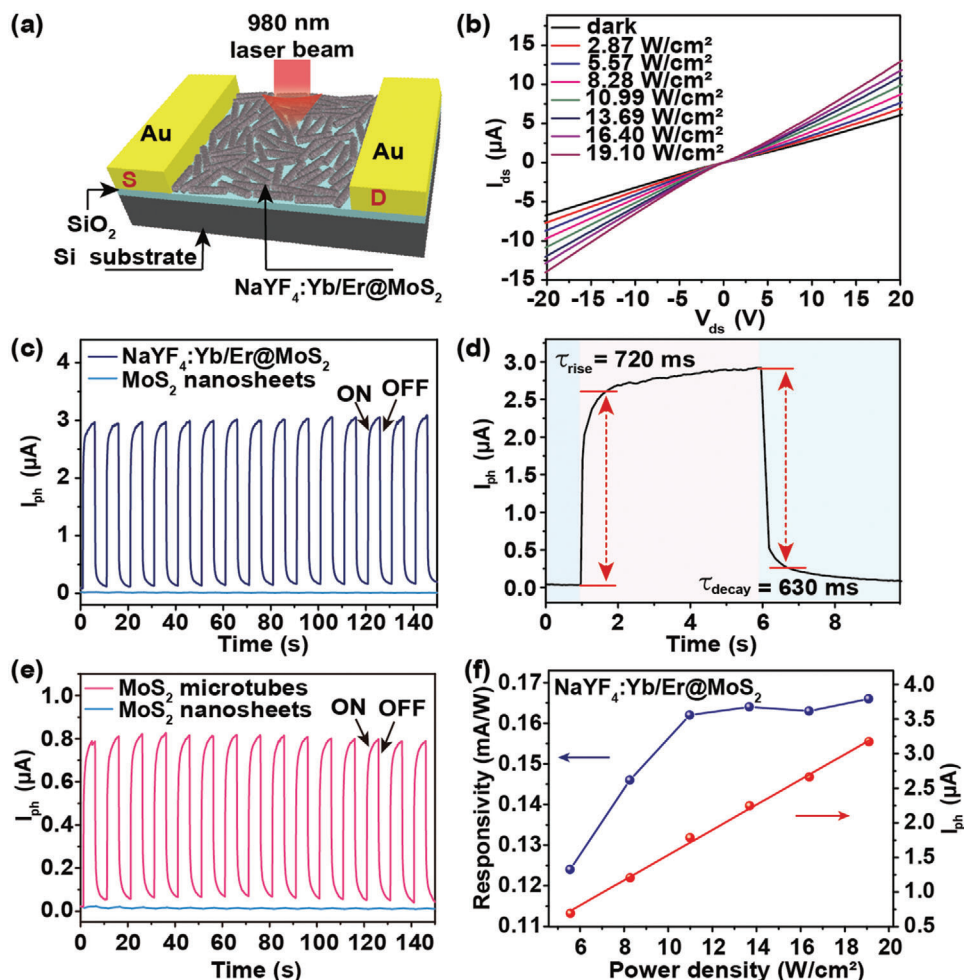


**Figure 3.** a) Schematic illustration of the optoelectronic device fabricated using NaYF<sub>4</sub>:Yb/Er@MoS<sub>2</sub> composite with channel length of 100 μm and width of 1000 μm. b) Dependence of the *I*–*V* curves on illumination power density of the device in (a), under 980 nm laser excitation. c) Temporal photocurrent responses of devices made of NaYF<sub>4</sub>:Yb/Er@MoS<sub>2</sub> and MoS<sub>2</sub> nanosheets, respectively. d) Time-resolved photocurrent indicating the rise and decay time after 980 nm laser switching ON or OFF. e) Temporal photocurrent responses of devices made of MoS<sub>2</sub> microtubes and MoS<sub>2</sub> nanosheets, respectively. f) Photocurrent and responsivity of NaYF<sub>4</sub>:Yb/Er@MoS<sub>2</sub> device as a function of illumination power density at 980 nm and voltage at 10 V.

observable, although greatly weakened (Figure 2c), which might be caused by the UCL reabsorption by MoS<sub>2</sub> as well as light scattering from small pieces of MoS<sub>2</sub>. Accordingly, shortening of emission lifetimes at 540 and 654 nm from 243 and 494 μs in NaYF<sub>4</sub>:Yb/Er to 182 and 416 μs in the composite, respectively, suggests the obvious ET from NaYF<sub>4</sub>:Yb/Er to MoS<sub>2</sub>, while no prominent lifetime change was detected in their physical mixture (Figure 2d,e). The efficiency of nonradiative ET process is estimated to be around 25% for <sup>4</sup>S<sub>3/2</sub> level and 15% for <sup>4</sup>F<sub>9/2</sub> level.<sup>[32]</sup> Figure 2f depicts the nonradiative ET pathways where the energy responsible for UCL emissions is transferred directly to the closely bound MoS<sub>2</sub> thin layers.<sup>[33]</sup> Moreover, the 1.276 eV bandgap of MoS<sub>2</sub> thin layers (Figure S10, Supporting Information) matches with both emissions at 540 and 654 nm of the microrods, which shall be responsible for the lifetime decrease (Figure 2d,e).

To showcase the improved NIR-response of 3D MoS<sub>2</sub> hollow architectures brought by the NIR-responsive template,<sup>[34]</sup> a pho-

todetector was fabricated (Figure 3a) using NaYF<sub>4</sub>:Yb/Er@MoS<sub>2</sub> composite shown in Figure 1d. The optical image of the photodetector is displayed in Figure S11a (Supporting Information), of which the channel length and width is 100 and 1000 μm, respectively. The thickness of NaYF<sub>4</sub>:Yb/Er@MoS<sub>2</sub> film is about 1 μm as shown in Figure S11b (Supporting Information). Current–voltage (*I*–*V*) measurements under dark and illumination conditions give linear characteristics at low voltage (Figure 3b), demonstrating a typical ohmic contact between the electrodes and the channel materials,<sup>[35]</sup> which makes bias voltage applied on the active channel rather than on the contact interface between electrode and channel material, and ensures high electrical responsivity. Comparison of Figure 3b and Figure S12 (Supporting Information) indicates that the dark current of the composite is much larger than that of pure MoS<sub>2</sub> nanosheets, suggesting higher electrical conductivity of the composite. The negative photoresponse in pure MoS<sub>2</sub> nanosheets (Figure S12, Supporting Information) is likely due to the competitive effects

between photogenerated charge carriers and photothermal effect.<sup>[36–38]</sup> It should be noted that *I-V* curves of photodetector made of pure MoS<sub>2</sub> nanosheets showed Schottky-contacted characteristics (Figure S12, Supporting Information), while that of NaYF<sub>4</sub>:Yb/Er@MoS<sub>2</sub> composite showed ohmic-contact features (Figure 3b), which was likely due to the 3D structure of NaYF<sub>4</sub>:Yb/Er@MoS<sub>2</sub> compared to 2D MoS<sub>2</sub> nanosheets. Because the special 3D framework makes MoS<sub>2</sub> contacted with metal electrode mostly in the way of “edge-contact,” while MoS<sub>2</sub> nanosheets mainly in the way of “top-contact” and the former style was recognized helpful for reducing contact resistance and improving electrical properties.<sup>[39–41]</sup>

As an important parameter for NaYF<sub>4</sub>:Yb/Er@MoS<sub>2</sub> photodetector, the temporal response was recorded under excitation of a pulsed laser with time interval of 10 s. The highly repeatable and stable photocurrent under 980 nm laser irradiation was evidently enhanced in NaYF<sub>4</sub>:Yb/Er@MoS<sub>2</sub> composite by 600 folds compared with that of pure MoS<sub>2</sub> nanosheets at the illumination power density of 19.10 W cm<sup>-2</sup> and voltage of 10 V (Figure 3c), which displays an excellent light switching functionality of this device. The time-resolved photocurrent rises accordingly with increased excitation power density or applied voltage (Figures S13 and S14, Supporting Information). The switching time for the photocurrent rise, defined as the time for the rise of the output signal from 0% to 90% of the maximal output value,<sup>[42]</sup> is 0.72 s for NaYF<sub>4</sub>:Yb/Er@MoS<sub>2</sub> photodetector (Figure 3d), while the one for decay, defined as the time for the decrease from the maximal output value to 10%, is 0.63 s (Figure 3d).

Only limited photocurrent can be generated in pure MoS<sub>2</sub> nanosheets under NIR (980 nm) excitation due to the comparatively large bandgap (1.276 eV). However, when the template NaYF<sub>4</sub>:Yb/Er was integrated in the photodetector, the synergetic effect derived from the 3D architecture of MoS<sub>2</sub> microtubes and non-radiative ET from NaYF<sub>4</sub>:Yb/Er greatly promotes the NIR photoresponse of MoS<sub>2</sub>. As a contrast, a 160-fold enhanced photoresponse was still obtained in photodetector made of MoS<sub>2</sub> microtubes (Figure 3e), which could be similarly attributed to the increased electric conductivity of the 3D structure compared with that of MoS<sub>2</sub> nanosheets.

MoS<sub>2</sub> can directly absorb illuminating photons above its band gap and generate charge carriers, and the photocurrent increases with the light intensity following the power-law of<sup>[43]</sup>

$$I_{\text{ph}} \propto I^m \quad (1)$$

in which  $I_{\text{ph}}$  is the current when light is ON and  $I$  is the emission intensity of the NIR light source, which can be directly absorbed by MoS<sub>2</sub>. For NaYF<sub>4</sub>:Yb/Er@MoS<sub>2</sub>,  $I$  should be the intensity of UCL emitted from NaYF<sub>4</sub>:Yb/Er microrods, which is proportional to the excitation laser power density

$$I \propto P_{\text{Ex}}^n \quad (2)$$

where  $n$  is defined as the number of photons required for UCL, and  $P_{\text{Ex}}$  is the laser power density. Therefore, it can be figured out that

$$I_{\text{ph}} \propto P_{\text{Ex}}^{mn} \quad (3)$$

So for NaYF<sub>4</sub>:Yb/Er@MoS<sub>2</sub> photodetector, through exponential fit shown in Figure 3f, the calculated  $mn$  is 1.14. The number of photons for green and red upconversion emissions were obtained by fitting the curve of emission intensity versus excitation power (Figure S15, Supporting Information). Because both green and red emissions can be absorbed by MoS<sub>2</sub>, we here applied the average photon number for green and red upconversion emission,  $n = 1.87$ . Therefore the calculated value for  $m$  is 0.61, which falls within the range of  $0 < m < 1$ , and suggests the typical semiconductor property involving electron–hole separation, trapping, and recombination.<sup>[44]</sup> Moreover, the NIR response of this photodetector can be further amplified  $\approx 1.8$  folds (Figure S16a, Supporting Information) by coupling with Au nanorods at dimensions of 15 nm  $\times$  95 nm (Figure S17, Supporting Information), whose localized surface plasmon resonance matches exactly with the excitation wavelength of NaYF<sub>4</sub>:Yb/Er at 980 nm (Figure S16b, Supporting Information). This result, again, proves not only the critical role that the template plays but also the rationality of our design principle.

To further evaluate the photoresponse performance, responsivity ( $R$ ), specific detectivity ( $D^*$ ), and external quantum efficiency (EQE) were evaluated.  $R$  represents the electric response to excitation light and is defined as  $I_{\text{ph}}/AP_{\text{Ex}}$ , where  $A$  is the effective area of the detector.  $D^*$  stands for the ability of a photodetector in detecting weak signals, and is defined as  $RA^{1/2}/(2eI_{\text{dark}})^{1/2}$ , where  $e$  is electron charge. EQE is defined as  $hcR/e\lambda$ , where  $h$  is the Planck constant,  $c$  is the light velocity.<sup>[35,43]</sup> Therefore we can deduce that the  $R$  of NaYF<sub>4</sub>:Yb/Er@MoS<sub>2</sub> photodetector kept increasing and reached steady state (Figure 3f) with laser power increasing. Moreover, compared with MoS<sub>2</sub> nanosheet photodetector,  $R$ ,  $D^*$ , and EQE are increased from  $0.268 \times 10^{-3}$  mA W<sup>-1</sup>,  $9.3 \times 10^4$  Jones and  $0.34 \times 10^{-4}\%$  to  $166 \times 10^{-3}$  mA W<sup>-1</sup>,  $560 \times 10^4$  Jones and  $210 \times 10^{-4}\%$ , respectively. Table S1 (Supporting Information) also summarized previously reported results where we can find that our work shows similar or even better performance. However, we believe that after further optimization of the material design parameters, fabrication steps, and working conditions, devices made of NaYF<sub>4</sub>:Yb/Er@MoS<sub>2</sub> composite shall exhibit even better NIR photoelectric detectivity.

Taking advantage of the multiple absorption capability of Er<sup>3+</sup>, the working wavelength of such photodetector can be readily tuned to another range. For example, in the photodetector made of NaYF<sub>4</sub>:Er@MoS<sub>2</sub> where Er<sup>3+</sup> is responsive to 1532 nm laser illumination (Figure S18, Supporting Information), a 276-fold photoresponse enhancement was obtained compared with that of pure MoS<sub>2</sub> nanosheets (Figure S19, Supporting Information). Similarly, this was also due to the ET from Er<sup>3+</sup> in the template to the MoS<sub>2</sub> shell (Figure S20, Supporting Information) according to the lifetime changes of the luminescence emissions at 540 and 654 nm (Figure S21, Supporting Information), with efficiency of 22% and 14%, respectively. The photodetector made of MoS<sub>2</sub> microtubes gave a 155-fold improvement (Figure S19, Supporting Information), which is almost identical to that of 160-fold shown in Figure 3e and confirms reliable quality of the MoS<sub>2</sub> microtubes though different templates were used, i.e., NaYF<sub>4</sub>:Yb/Er versus NaYF<sub>4</sub>:Er. It needs to be pointed out that although under the same laser illumination power density, it is reasonable to see smaller photocurrent in NaYF<sub>4</sub>:Er@MoS<sub>2</sub> photodetector under 1532 nm laser illumination (Figure S19,

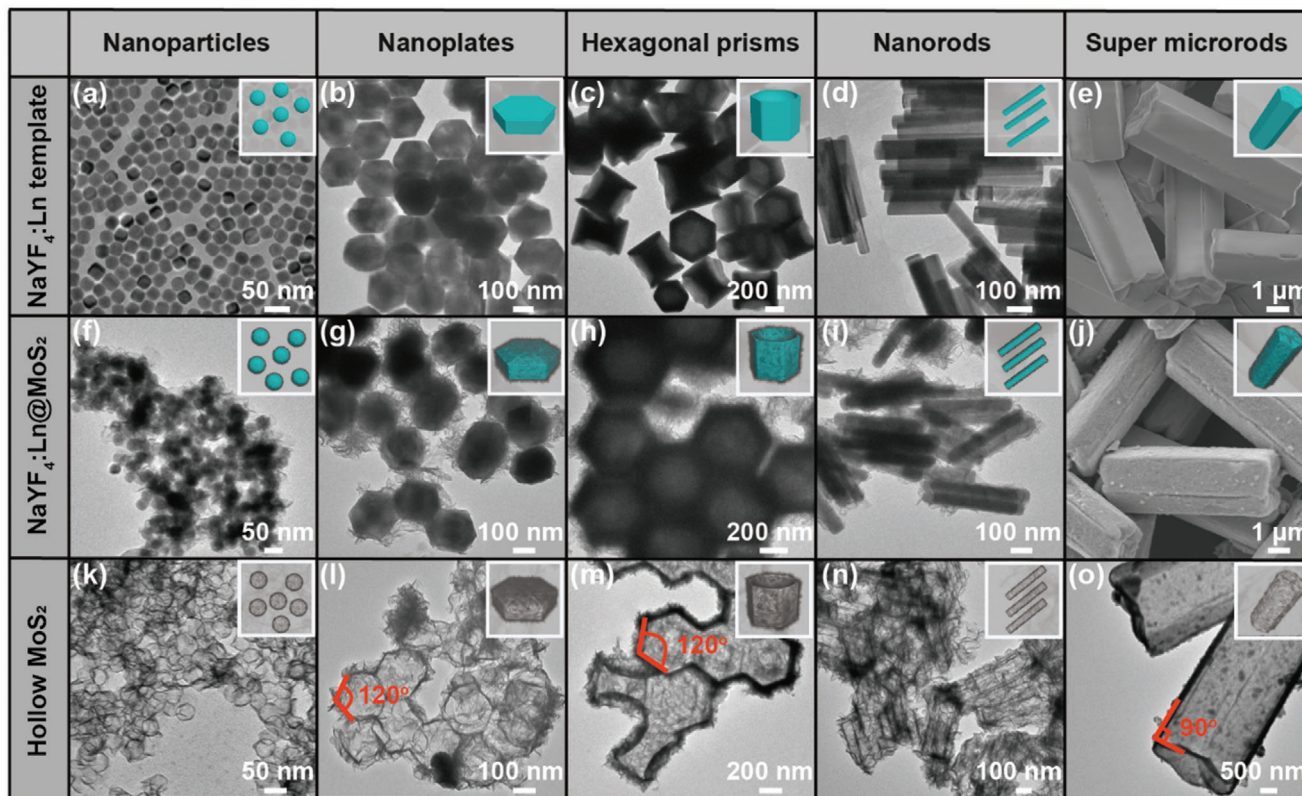


**Figure 4.** TEM images of  $\text{NaYF}_4:\text{Ln}$  with morphologies of a) nanoparticle, b) nanoplate, c) hexagonal prism, d) nanorod, and e) super microrod, which were used as templates for growing of corresponding composites showing in (f–j). k–o) are TEM images of the corresponding hollow  $\text{MoS}_2$  architectures after template removal.

Supporting Information) compared with that of  $\text{NaYF}_4:\text{Yb}/\text{Er}@\text{MoS}_2$  excited with 980 nm laser (Figure 3c) because: 1)  $\text{Er}^{3+}$  has smaller absorption cross section ( $1.7 \times 10^{-21} \text{ cm}^2$  at 1532 nm) in  $\text{NaYF}_4:\text{Er}$  than that of  $\text{Yb}^{3+}$  ( $9.11 \times 10^{-21} \text{ cm}^2$  at 980 nm) in  $\text{NaYF}_4:\text{Yb}/\text{Er}$ ,<sup>[33]</sup> and 2) the relatively low upconversion efficiency of  $\text{Er}^{3+}$  in  $\text{NaYF}_4:\text{Er}$ , which is a 3-photon upconversion process compared with a 2-photon process in  $\text{NaYF}_4:\text{Yb}/\text{Er}$ .

Due to the very close ionic radii and highly similar chemical properties of lanthanide ions,  $\text{Gd}^{3+}$  was intentionally codoped for more sophisticated dimension and morphology tuning of the templates. Following the same recipe, a wide variety of  $\text{MoS}_2$  hollow architectures could then be readily obtained when  $\text{NaYF}_4:\text{Ln}$  ( $\text{Ln} = \text{Yb}/\text{Er}$ , 18/2 mol% for nanoparticles, nanoplates, hexagonal prisms, and super microrods;  $\text{Ln} = \text{Yb}/\text{Er}/\text{Gd}$ , 18/2/30 mol% for nanorods) with pre-designed dimensions and morphologies were used as templates (Figure 4), such as nanovesicles as small as 35 nm (Figure 4a,f,k), hollow hexagonal prisms with height varying from 50 (Figure 4b,g,l) to 240 nm (Figure 4c,h,m), nanotubes (Figure 4d,i,n), and super microtubes (Figure 4e,j,o), respectively. Detailed analysis of TEM images of the nanovesicles indicates only  $\approx 2.5$  nm average thickness of the  $\text{MoS}_2$  shell (Figure S22, Supporting Information), which is so far the smallest value ever reported. Moreover, it is worth emphasizing that not only the thin layer grows very uniformly along the templates, the structural details such as the  $120^\circ$  internal angle (Figure 4l,m) of

the hollow hexagonal prism, and the sharp end of the super microtube (Figure 4o) derived from respective templates, were also perfectly retained in the hollow architectures. This, on the other hand, reflects perfect control for high quality hollow architecture synthesis originated from the sufficient affinity between  $\text{MoS}_2$  and  $\text{NaYF}_4:\text{Ln}$ , and introduction of  $\text{Gd}^{3+}$  does not affect the quality of the composite or template removal. Such widely designable hollow architectures may possess great potentials in drug delivery, energy storage, thin film separation, as well as electrochemical and/or photocatalysis.

In conclusion, we have developed a facile and reliable template-based strategy for arbitrary construction of hollow  $\text{MoS}_2$  architectures with dimensions ranging from as small as  $\approx 35$  nm to up to as large as  $\approx 10 \mu\text{m}$ , and morphologies ranging from nanoscaled vesicles to micro-sized tubes. This is the first time that easy fabrication of various  $\text{MoS}_2$  hollow structures with shells as thin as  $\approx 2.5$  nm was ever accessed. As an added value, the lanthanide template is able to upconvert the NIR excitation energy and transfer efficiently to the  $\text{MoS}_2$  shell, which can be further exploited for the development of multichannel NIR photodetectors. Moreover, the strategy developed here should inspire further constructions of other TMD hollow architectures with outstanding performances not only in optoelectronics, but also potentially in energy storage and photo-/electrochemical catalysis, which are ongoing projects in our lab.

## Supporting Information

Supporting Information is available from the Wiley Online Library or from the author.

## Acknowledgements

C.G. and Y.H. contributed equally to this work. This work is supported by National Natural Science Foundation of China (No. 21371095), Jiangsu Key Research and Development Program (No. BE2015699), Young Elite Scientists Sponsorship Program by CAST (No. 2017QNRC001), Natural Science Foundation of Jiangsu Province (No. BK20160987), and the Qing Lan Project of Jiangsu Province.

## Conflict of Interest

The authors declare no conflict of interest.

## Keywords

energy transfer, hollow MoS<sub>2</sub>, near-infrared, template, upconversion luminescence

Received: June 29, 2020

Revised: August 2, 2020

Published online: October 15, 2020

- [1] Q. Lu, Y. Yu, Q. Ma, B. Chen, H. Zhang, *Adv. Mater.* **2016**, *28*, 1917.
- [2] C. Zhao, X. Wang, J. Kong, J. M. Ang, P. S. Lee, Z. Liu, X. Lu, *ACS Appl. Mater. Interfaces* **2016**, *8*, 2372.
- [3] M. Acerce, D. Voiry, M. Chhowalla, *Nat. Nanotechnol.* **2015**, *10*, 313.
- [4] G. Li, D. Zhang, Q. Qiao, Y. Yu, D. Peterson, A. Zafar, R. Kumar, S. Curtarolo, F. Hunte, S. Shannon, Y. Zhu, W. Yang, L. Cao, *J. Am. Chem. Soc.* **2016**, *138*, 16632.
- [5] Q. He, Z. Zeng, Z. Yin, H. Li, S. Wu, X. Huang, H. Zhang, *Small* **2012**, *8*, 2994.
- [6] S. Bertolazzi, D. Krasnozhan, A. Kis, *ACS Nano* **2013**, *7*, 3246.
- [7] Z. Zeng, Z. Yin, X. Huang, H. Li, Q. He, G. Lu, F. Boey, H. Zhang, *Angew. Chem. Int. Ed.* **2011**, *50*, 11093.
- [8] B. Radisavljevic, A. Radenovic, J. Brivio, V. Giacometti, A. Kis, *Nat. Nanotechnol.* **2011**, *6*, 147.
- [9] W. Choi, M. Y. Cho, A. Konar, J. H. Lee, G. B. Cha, S. C. Hong, S. Kim, J. Kim, D. Jena, J. Joo, *Adv. Mater.* **2012**, *24*, 5832.
- [10] X. Duan, C. Wang, J. C. Shaw, R. Cheng, Y. Chen, H. Li, X. Wu, Y. Tang, Q. Zhang, A. Pan, J. Jiang, R. Yu, Y. Huang, X. Duan, *Nat. Nanotechnol.* **2014**, *9*, 1024.
- [11] X. Zhang, Z. Lai, C. Tan, H. Zhang, *Angew. Chem. Int. Ed.* **2016**, *55*, 8816.
- [12] J. H. Han, M. Kwak, Y. Kim, J. Cheon, *Chem. Rev.* **2018**, *118*, 6151.
- [13] M. Wang, G. Li, H. Xu, Y. Qian, J. Yang, *ACS Appl. Mater. Interfaces* **2013**, *5*, 1003.
- [14] Q. Yun, Q. Lu, X. Zhang, C. Tan, H. Zhang, *Angew. Chem. Int. Ed.* **2018**, *57*, 626.
- [15] L. Cong, H. Xie, J. Li, *Adv. Energy Mater.* **2017**, *7*, 1601906.
- [16] Y. Li, R. Zhang, W. Zhou, X. Wu, H. Zhang, J. Zhang, *ACS Nano* **2019**, *13*, 5533.
- [17] S. Zhuo, Y. Xu, W. Zhao, J. Zhang, B. Zhang, *Angew. Chem. Int. Ed.* **2013**, *125*, 8764.
- [18] X. Yu, Y. Feng, Y. Jeon, B. Guan, X. Lou, U. Paik, *Adv. Mater.* **2016**, *28*, 9006.
- [19] X. Liu, R. Deng, Y. Zhang, Y. Wang, H. Chang, L. Huang, X. Liu, *Chem. Soc. Rev.* **2015**, *44*, 1479.
- [20] X. Wang, H. Chang, J. Xie, B. Zhao, B. Liu, S. Xu, W. Pei, N. Ren, L. Huang, W. Huang, *Coord. Chem. Rev.* **2014**, *273*, 201.
- [21] Y. Han, H. Li, Y. Wang, Y. Pan, L. Huang, F. Song, W. Huang, *Sci. Rep.* **2017**, *7*, 1320.
- [22] X. Teng, Y. Zhu, W. Wei, S. Wang, J. Huang, R. Naccache, W. Hu, A. L. Y. Tok, Y. Han, Q. Zhang, Q. Fan, W. Huang, J. A. Capobianco, L. Huang, *J. Am. Chem. Soc.* **2012**, *134*, 8340.
- [23] Z. Yuan, L. Zhang, S. Li, W. Zhang, M. Lu, Y. Pan, X. Xie, L. Huang, W. Huang, *J. Am. Chem. Soc.* **2018**, *140*, 15507.
- [24] P. Wang, H. Sun, Y. Ji, W. Li, X. Wang, *Adv. Mater.* **2014**, *26*, 964.
- [25] H. Hwang, H. Kim, J. Cho, *Nano Lett.* **2011**, *11*, 4826.
- [26] Y. R. Lim, W. Song, J. K. Han, Y. B. Lee, S. J. Kim, S. Myung, S. S. Lee, K. S. An, C. J. Choi, J. Lim, *Adv. Mater.* **2016**, *28*, 5025.
- [27] W. Kong, T. Sun, B. Chen, X. Chen, F. Ai, X. Zhu, M. Li, W. Zhang, G. Zhu, F. Wang, *Inorg. Chem.* **2017**, *56*, 872.
- [28] R. G. Pearson, *Science* **1966**, *151*, 172.
- [29] Y. Ding, J. Gu, T. Zhang, A. Yin, L. Yang, Y. Zhang, C. Yan, *J. Am. Chem. Soc.* **2012**, *134*, 3255.
- [30] Y. Zhang, L. Huang, X. Liu, *Angew. Chem. Int. Ed.* **2016**, *55*, 5718.
- [31] R. J. Kula, *Anal. Chem.* **1966**, *38*, 1382.
- [32] P. A. Tanner, L. Zhou, C. Duan, K. L. Wong, *Chem. Soc. Rev.* **2018**, *47*, 5234.
- [33] B. Yang, Y. Wang, T. Wei, Y. Pan, E. Zhou, Z. Yuan, Y. Han, M. Li, X. Ling, L. Yin, X. Xie, L. Huang, *Adv. Funct. Mater.* **2018**, *28*, 1801782.
- [34] C. Strohöhöfe, A. Polman, *Opt. Mater.* **2003**, *21*, 705.
- [35] P. T. Gomathi, P. Sahatiya, S. Badhulika, *Adv. Funct. Mater.* **2017**, *27*, 1701611.
- [36] L. Guo, X. Wang, L. Feng, X. Zheng, G. Chen, X. Yang, F. Xu, N. Tang, L. Lu, W. Ge, B. Shen, *Appl. Phys. Lett.* **2013**, *102*, 072103.
- [37] J. Miao, B. Song, Q. Li, L. Cai, S. Zhang, W. Hu, L. Dong, C. Wang, *ACS Nano* **2017**, *11*, 6048.
- [38] P. C. Wei, S. Chattopadhyay, M. D. Yang, S. C. Tong, J. L. Shen, C. Y. Lu, H. C. Shih, L. C. Chen, K. H. Chen, *Phys. Rev. B* **2010**, *81*, 045306.
- [39] H. Xu, X. Han, X. Dai, W. Liu, J. Wu, J. Zhu, D. Kim, G. Zou, K. A. Sablon, A. Sergeev, Z. Guo, H. Liu, *Adv. Mater.* **2018**, *30*, 1706561.
- [40] A. Allain, J. Kang, K. Banerjee, A. Kis, *Nat. Mater.* **2015**, *14*, 1195.
- [41] J. Kang, D. Sarkar, W. Liu, D. Jena, K. Banerjee, *Int. Electron Dev. Meet.* **2012**, 407.
- [42] F. Li, H. Wang, D. Kufer, L. Liang, W. Yu, E. Alarousu, C. Ma, Y. Li, Z. Liu, C. Liu, N. Wei, F. Wang, L. Chen, O. F. Mohammed, A. Fratalocchi, X. Liu, G. Konstantatos, T. Wu, *Adv. Mater.* **2017**, *29*, 1602432.
- [43] Y. Zhang, J. Wang, B. Wang, J. Shao, J. Deng, C. Cong, L. Hu, P. Tian, R. Liu, S. L. Zhang, Z. J. Qiu, *Adv. Optical Mater.* **2018**, *6*, 1800660.
- [44] M. Hafeez, L. Gan, H. Li, Y. Ma, T. Zhai, *Adv. Mater.* **2016**, *28*, 8296.